Combustion and Flame 265 (2024) 113505

Contents lists available at ScienceDirect

Combustion and Flame

journal homepage: www.sciencedirect.com/journal/combustion-and-flame

Flame wrinkling and self-disturbance in cellularly unstable hydrogen-air laminar flames

Yu Xie, Junfeng Yang *, Xiaojun Gu

School of Mechanical Engineering, University of Leeds, Leeds LS2 9JT, United Kingdom

ARTICLE INFO

Keywords:
PIV
Flame instability
Self-acceleration
Self-disturbance

ABSTRACT

Particle image velocimetry (PIV) was employed to investigate the disturbance of unstable laminar hydrogen-air outwardly propagating spherical flames in a spherical explosion vessel. Both the flame speed and gas velocities exhibit acceleration due to the wrinkled flame surface. This acceleration occurs throughout the cycle of strong and weak acceleration phases, which is driven by the division and expansion of cells across the flame front. The flame speed acceleration exponent, α, and the gas velocity ahead of the flame acceleration exponent, α_g, are nearly identical. This suggests a close interrelation between the self-acceleration of flame speed (S_n) and the gas velocity ahead of the flame front (u_g). Stronger gas flow disturbances caused by more wrinkly flame surfaces are associated with smaller cell sizes. Furthermore, the power spectral density displayed by the flow ahead of the flame front shows remarkable similarity to the fluctuation observed in the flame front. This suggests that the driver for gas disturbance generated ahead of the flame front can be attributed to the wrinkled flame front, whether arising from flame instability. The Power Spectral Density (PSD) of gas velocities and flame wrinkling display a steeper slope (-2.7) compared to isotropic turbulence within the inertial sub-range, where energy spectra decay at -5/3, as measured in a previous study. This observation suggests that gas flow induced by flame instability differs from isotropic turbulence. The normalized gas flow disturbance intensity, $(\overline{u'_{gc}}/u_{gc})$, has been proposed as an evaluation parameter for studying intrinsic disturbance intensity. The increased gas flow disturbance intensity is closely associated with both the wrinkled flame surface and a smaller cell size. Empirical correlations for gas flow disturbance intensity are explored in terms of the laminar critical Karlovitz number (K_{cl}), effective Lewis number (Le_{eff}), and burnt gas Markstein number (Ma_b). There is no obvious causal link between self-acceleration and self-disturbance. Both phenomena are attributed to the wrinkled flame surface.

Novelty and significance

This research contributes to the understanding of self-disturbance in laminar hydrogen-air flames through the utilization of Particle Image Velocimetry (PIV). The novelty of the present work includes a unique methodology for obtaining unburnt gas velocity and the introduction of a novel dimensionless group, $(\overline{u'_{gc}}/u_{gc})$, for assessing the intensity of disturbances in the unburnt gas velocity. A combination of the PIV technique and the theoretical mass conservation method is employed to derive the unburnt gas velocity ahead of the flame front. This approach addresses the limitation of the PIV method, which could not resolve the flow field close to the highly cellular flame front.The power spectral density of the flow preceding the flame front exhibits a remarkable similarity to the fluctuation pattern observed in the flame front itself. The results imply that the gas flow preceding the flame front may not be strictly characterized as turbulent flow. In addition, the observation suggests there is no direct correlation between self-acceleration and self-disturbance. Both phenomena are attributed to the wrinkled flame surface.

1. Introduction

In many instances, hydrogen generated from nuclear waste (via radiolysis) is collected in a storage vessel or product container at nuclear power plants. When mixed with air, these hydrogen-air mixtures have the potential to ignite, leading to damaging overpressures through deflagration or detonation. The risk of hydrogen detonation in nuclear plants is particularly concerning as it could damage the piping system, resulting in the leakage of radioactive material and potential environmental hazards. Even if detonation does not occur, the initial flame

* Corresponding author.
E-mail address: J.Yang@leeds.ac.uk (J. Yang).

https://doi.org/10.1016/j.combustflame.2024.113505
Received 13 June 2023; Received in revised form 4 May 2024; Accepted 7 May 2024
Available online 15 May 2024

Nomenclature

A	empirical constant
A_g	empirical constant for u_g
A_L	mean spherical flame surface area (m^2)
A_T	total/instantaneous spherical flame surface area (m^2)
B	flame speed pulsation amplitude (m/s)
B_g	gas velocity pulsation amplitude (m/s)
c_p	specific heat (J/kg/K)
d	fractal excess
d_g	fractal excess for u_g
D	fractal dimension of the flame edge
E_a	activation energy (J)
f	frequency of flame speed (s^{-1})
f_g	frequency of gas velocity (s^{-1})
g	fluctuation of the flame front
k	wave number (mm^{-1})
Ka	Karlovitz number
K_{cl}	critical Karlovitz number
L	wavelength (mm)
L_b	flame burnt gas Markstein length (mm)
Le	Lewis number
Le_E	Lewis number of excessive reactants
Le_D	Lewis number of deficient reactants
Le_{eff}	effective Lewis number
Ma	Markstein number
Ma_b	flame burnt gas Markstein number
N_p	total number of velocity vectors in one annulus
n_{max}	maximum wavenumber (mm^{-1})
P	pressure (MPa)
P_i	initial pressure (MPa)
$P0$	0.1 MPa
P_T	perimeter of 2D wrinkled flame (mm)
Pe	Peclet number
Pe_{cl}	critical Peclet number
Pr	Prandtl number
r	flame radius (mm)
r_b	flame burnt front radius (mm)
r_{max}	maximum flame radius (mm)
r_u	mean flame cold front radius (mm)
R_i	flame radius at i^{th} local sector (mm)
r_{PIV}	flame front radius obtained in PIV photography (mm)
R_T	equated wrinkled flame front radius (mm)
R^o	gas constant (J/(K·mol))
S_n	flame speed (m/s)
$S_g(k)$	PSD of gas velocities adjacent to flame front
$S_f(k)$	PSD of wrinkling amplitudes of flame front
t	time after spark ignition (s)
T_b	adiabatic burnt gas temperature (K)
T_u	unburnt fresh gas temperature (K)
T_i	initial temperature (K)
T_P	seeding particle evaporation temperature (K)
u_g	gas velocity (m/s)
u_{gc}	mean u_g using continuity conservation in one annulus (m/s)
u_{gp}	mean u_g using polynomial fitting in one annulus (m/s)
u_{gs} u_g	derived from 1-D code simulation (m/s)
u_r	unburnt gas velocity (m/s)
$u_{gc}^{'}$	spatial root mean square (RMS) gas velocity (m/s)
$u(x,y)$	velocity component in the x-direction (m/s)
$v(x,y)$	velocity component in the y-direction (m/s)
X	function of time in the continuity equation, Eq. (9)
Ze	Zel'dovich number

Greek symbols

α	acceleration exponent
α_{cl}	the flame stretch rate at the critical point (1/s)
α_f	flame stretch rate (1/s)
α_g	acceleration exponent for u_g
α_{td}	thermal diffusivity (m^2/s)
δ	flame thickness (mm)
λ	phase difference of flame speed
λ_g	phase difference of gas velocity
ρ	density (kg/m^3)
ρ_b	the density of the burnt gas (kg/m^3)
ρ_u	the density of the unburnt gas (kg/m^3)
σ	ratio of unburned gas density to burned gas density ρ_u/ρ_b
ϕ	equivalence ratio
Φ	mass of excess to deficient reactants in the fresh mixture relative to their stoichiometric ratio
Λ	wavelength (mm)
Λ_{min}	minimum wavelength (mm)
Λ_{max}	maximum wavelength (mm)
Γ	constant Pe/n_{max}, normalised cell size (mm)

acceleration and the generated overpressure pose severe hazards. Understanding the development of hydrogen flame instabilities and the extent of their regimes is crucial for better hydrogen safety management. Darrieus-Landau (DL)/hydrodynamic and thermal diffusion (TD) instabilities play important roles in transforming stable flames into unstable ones, manifesting as flame wrinkling and an associated increasing rate of burning. Eventually, the flame starts to self-accelerate due to the increased flame surface area [1,2]. Moreover, there is a proposed concept that a self-accelerating flame, along with an increasingly wrinkled flame surface, might exhibit 'turbulence-like' behavior. The neighboring flow could show potential characteristics of turbulence, a phenomenon known as self-turbulization [3], which could then transition to supersonic speed through a process known as deflagration-to-detonation transition (DDT) [4]. Fractal theory [4,5] and related experiments [6–8], including large atmospheric explosions with flame sizes of several meters [9–11], have been conducted to deepen our understanding of self-acceleration or self-turbulization.

The acceleration exponent, α, for unstable expanding flames, is introduced to describe the relationship between flame radius and time after ignition using the power equation, given by $r_u = At^{\alpha}$, r_u is the mean flame cold front radius, t is the time after spark ignition, α is the acceleration exponent. The correlation of the accelerated flame propagation speed, S_n, and its acceleration exponent, α can be derived as:

$$S_n = \frac{dr_u}{dt} = A\alpha t^{\alpha-1} = A^{\frac{1}{\alpha}}\alpha(r_u)^{\frac{\alpha-1}{\alpha}} \sim {r_u}^d \tag{1}$$

where A is the empirical constant, and the fractal excess d is correlated with α via $d = (\alpha - 1)/\alpha$. Some researchers [12–14] have also found that hydrodynamically unstable flames exhibit fractal characteristics, whereas diffusive-thermally unstable flames do not. The fractal nature of hydrodynamically unstable flames is ascribed to their hierarchical structure. In contrast, diffusive-thermally unstable flames do not display fractal attributes due to the selective growth of wrinkles with specific wavelengths.

It is worth noting that recent studies have placed emphasis on global pulsation analysis. In these studies[11], global pulsation models have been developed to capture the phenomenon of global pulsation of flame speed, which arises from the continuous growth and splitting of cells. In

order to account for the pulsatory behaviour, a new term representing a sinusoidal function has been introduced to augment the existing power-law correlation:

$$S_n = A\alpha t^{\alpha-1} + B\sin(2\pi ft + \lambda) \quad (2)$$

where f is frequency(s^{-1}), B is amplitude (m/s) and λ is phase difference. Although various values of α were reported in previous theoretical and experimental studies [2,15–17], the results are diverse even for the same condition due to different extraction methods.

The Particle Image Velocimetry (PIV) technique can provide detailed gas vectors of the expansion flame [18–22]. In addition to capturing the temporal evolution of the flame cold front, S_n, the rate of entrainment of cold unburnt gas by the flame front (fresh gas velocity at the entrance of the flame front, ug) can be simultaneously derived. PIV enables a better understanding of the role of unburnt gas during the self-acceleration of premixed laminar flames. A conceptual premixed flame structure at a given instant during spherical explosive propagation is illustrated in Fig. 1 (left). The temperature profile and gas velocity profile in the radial direction (Fig. 1, right) were predicted using a 1D spherical flame code [23] with detailed hydrogen combustion kinetics (GRI-Mech 3.0) [24].

The turbulence-like structure of a laminar unstable flame after instability raises the intriguing question of whether Darrieus-Landau (DL) and thermal diffusion (TD) instabilities can induce disturbance or even turbulence within a premixed flame brush or even further into the gas flow, and to what extent and how strong. The theoretical groundwork for flame instability was laid by Landau, and subsequent studies followed [4–11]. Karlovitz et al. [26] and Scurlock and Grover [27] made significant progress by proposing the concept of flame-induced turbulence. The issue of flame-generated turbulence became a focal point of combustion community research, initially suggesting no occurrence. Later, it was discovered that higher turbulence occurs due to flame expansion but is quickly damped out as the distance from the flame front increases [28]. Two-dimensional laminar flames including vortex–flame interaction were studied in Bell et al. [29] and emissions from laminar diffusion flames in Bell et al. [30] and Sullivan et al. [31]. Ahmed and Prosser [32] studied flame-turbulence interaction and offered an alternative approach to modeling the physics using Reynolds-averaged Navier-Stokes (RANS) simulation. Flame-induced turbulence, studied through Large Eddy Simulation (LES), leads to the formation of many vortex pairs, which is the main source of large flame wrinkles [33,34]. Direct numerical simulation (DNS) has also been widely employed in flame-turbulence interaction [35–41]. However, Lipatnikov et al. [38] used DNS on a statistically stationary, 1D, planar, weakly turbulent, premixed flame and found that the effect of flame-generated turbulence on the burning rate appears fundamentally distinct from the effect of turbulence in the entering reactants on the rate. Aspden et al. [39] conducted a comprehensive study on the impact of turbulence on lean premixed hydrogen flames in an idealized scenario, employing high-resolution three-dimensional simulations. They observed that elevated turbulence levels amplify peak local burning rates and overall turbulent flame speeds. Subsequently, in their study [40], they utilized high-resolution direct numerical simulations to investigate turbulence-chemistry interaction in lean premixed hydrogen flames. They discovered that fuel consumption is notably intensified in regions characterized by positive curvature. Additionally, in another work [41], they delineated characteristics of chemistry-turbulence interactions specific to the pyrolysis of large-molecule fuels.

Various computational and experimental efforts have been made to study this classic yet poorly understood phenomenon. Videto et al. [42] used Laser Doppler Velocimetry (LDV) to study the competition between a propane-air flame and incident turbulence, showing increased turbulence intensity. Chaudhuri et al. [43] used high-speed particle image velocimetry measurements to quantify flame-turbulence interaction in centrally-ignited constant-pressure premixed flames. Peters [44] reported that radial flame propagation changes the original cold flow turbulence with statistical analysis, and Bradley et al. [45] demonstrated that a strong outwards velocity pulse can create extra ‘combustion turbulence’ as a result of the combined effects of a fast-burning rate and rapid volumetric expansion.

Liu et al. [3] demonstrated, through scaling analysis facilitated by Particle Image Velocimetry (PIV), that the observed spectra of energy are predominantly governed by the fractal nature characterizing the topological properties of the unstable cellular flame front. These studies suggest that flame expansion could alter the original turbulence flow or even create extra turbulence directly or indirectly. However, the detailed process of how an originally stable laminar flame self-accelerates and undergoes self-turbulization is of interest. Additionally, studying the link between acceleration exponents and turbulence or disturbance strength is necessary to understand the connection between self-acceleration and self-turbulization.

Given the above considerations, the present study aims to investigate

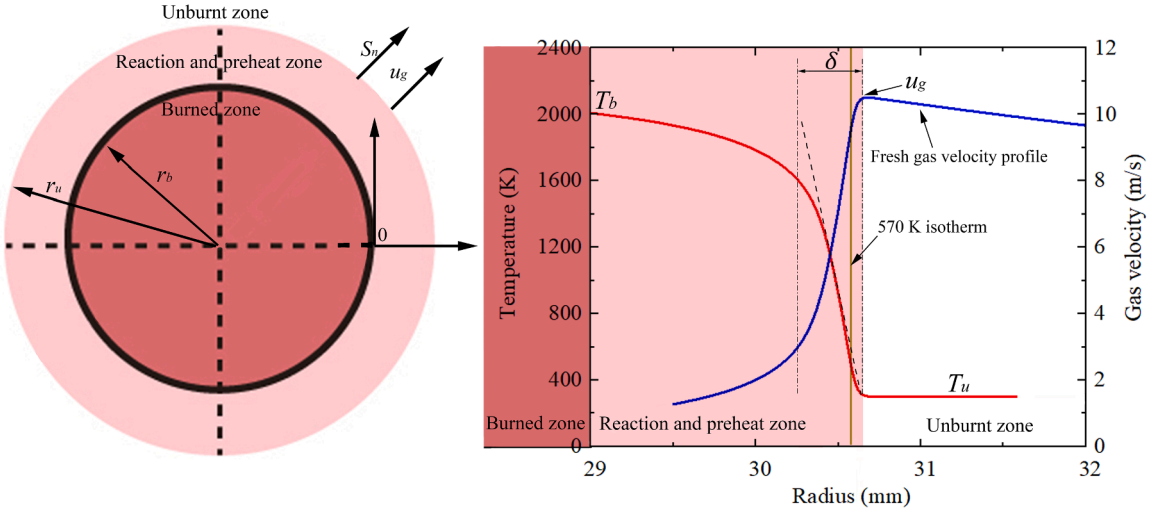

Fig. 1. Conceptual fresh gas velocity profile near the flame front of spherically propagation flame at r_u = 30.6 mm, P_i = 0.1 MPa, T_i = 300 K, ϕ = 1.0 using 1D spherical flame code [23] with detailed kinetic schemes [24]. The right figure is the detailed schematic diagram of flame propagation with an enlarged flame thickness. r_u is the mean flame cold front radius (mm), defined as the isotherm that is 5 K above the temperature of reactants [25], r_b is the mean flame hot front radius (mm), defined as the isotherm that is the temperature of products. The 570 K isotherm (yellowish-brown line) is the evaporation temperature of olive oil seeding particles used in PIV technique. T_b is the burnt gas temperature (K). T_u is the unburnt fresh gas temperature (K). δ is the flame thickness (mm).

the gas flow characteristics of expanding spherical flames in the hydrogen-air mixture, along with its self-accelerating propagation and self-turbulization phenomenon using small laboratory explosions. The details of the study include: (i) Exploring the self-accelerating phenomenon of flame propagation speed and gas velocity ahead of the flame front. Additionally, evaluating the acceleration exponents of flame speeds and gas velocities in the self-similar regime to understand their intrinsic relationship. (ii) Determining whether a freely propagating laminar flame may grow into a turbulent flame and investigating the consequences this transformation would have on the flow ahead of the flame front. (iii) Utilizing dimensionless groups to study and comprehend the intrinsic disturbance induced by a wrinkled hydrogen-air flame surface due to instability based on the variations of the unburnt gas velocity ahead of the flame. (iv) Investigating whether there is a direct relationship between self-acceleration and self-turbulization (or self-disturbance).

2. Experimental apparatus

The PIV setup in this study comprises several subsystems: MK-II combustion vessel, optical diagnostics, synchronization, and image data processing. Fig. 2 illustrates the PIV setup and data processing for flame speed measurements and gas vector calculations.

2.1. MK-II combustion vessel

The explosions occurred in a stainless steel explosion vessel (MK-II) with a 190 mm inner radius and orthogonal windows of 150 mm diameter. To meet the requirements, one electric heater (2 kW) was installed on the inside wall of the bomb to warm the vessel and air-fuel mixture. The temperature of the mixture was measured using a sheathed chrome alumina thermocouple, and mixing was facilitated by four electric-powered fans near the vessel inside the casing. A central spark plug was used, supplied by a 12 V transistorized automotive ignition coil.

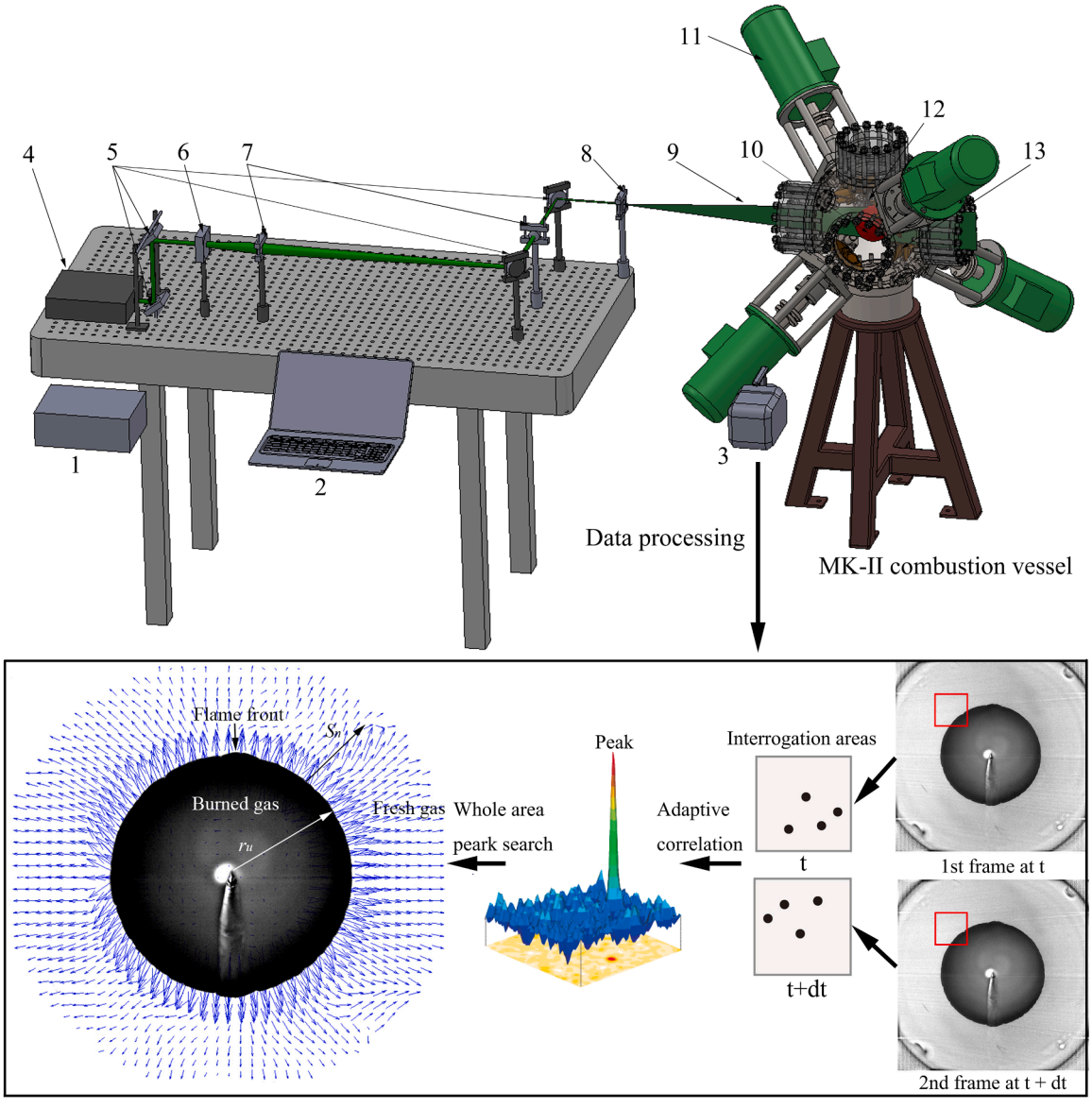

Fig. 2. Schematic of MK-II vessel (translucent display) and its auxiliary systems with PIV setup. Item 1: timer box; 2: computer; 3: camera; 4: Nd:YAG laser (DM60–532-DH); 5: periscopes; 6: plano-concave lens; 7: bi-convex spherical lens; 8: plano-concave cylindrical lens; 9: laser sheet; 10: flame; 11: motors; 12: heater; 13: fans. The section within a rectangular black line is 2D gas field calculation of PIV flame image and gas vectors using adaptive correlation. Optical windows are not displayed for a better illustration of the laser path.

2.2. Optical diagnostics and synchronization

In this study, olive oil was chosen as the seeding particles with a density of 920 kg/m^3. The tracer particles are generated by six jet atomisers (9010F0021, Dantec) and mixed with air in the intake pipes before they are introduced into the combustion vessel. The generated olive oil droplets have a diameter of approximately 1 μm and a boiling temperature of 570 K [20]. Previous studies demonstrated that the olive oil particles follow the fluid flow without lag while also offering good scattering light intensity [19–22]. Experimental tests demonstrated that the introduction of a small quantity of seeding particles had no significant impact on the combustion process [20]. These particles were illuminated twice in a brief time interval on a designated plane at the center of the vessel using a double-pulse laser light sheet through a side window of the combustion vessel, as shown in Fig. 2. A double-pulsed Nd:YAG laser (DM60–532-DH, Photonics Industries) producing a 532 nm wavelength green light laser beam with a maximum beam energy of 12 mJ was employed to illuminate the flow field. Due to the high propagation speed of the hydrogen-air flame, the repetition rate of the laser was set at 30 kHz for hydrogen while only 5 kHz for methane, isooctane, and n-heptane. The laser beam was expanded to a thin sheet with a thickness of around 0.5 mm using a series of optics lenses, as shown in Fig. 2. The optics consisted of a plano-concave and two bi-convex spherical lenses with focal lengths of −300 and 650 mm, a plano-concave cylindrical lens with a focal length of −20 mm, and four periscopes. The laser direction can be adjusted using four periscopes. Furthermore, the bi-convex spherical lens focused the beam on the center of the vessel, while the cylindrical lens enlarged the beam in one dimension, resulting in the formation of a thin sheet of light across a plane in the middle of the vessel. The spacing of three spherical lenses allowed the thickness of the light sheet to be regulated and altered. A high-speed camera pointed perpendicular to the laser sheet recorded the light scattered from the tracer particles. It captured a 12-bit picture pair of 768×768 pixels at a frequency of 5 kHz (methane, iso-octane, and n-heptane) and 30 kHz (hydrogen) with a pixel size of 0.222 mm/pixel. A computer-controlled synchronizer, PIV timer box (Dantec, model 80N77), was used, which controls the laser pulses, camera, and computer as an integrated automated system.

2.3. Data processing

The 'laser sheet visualization' approach utilized Mie-scattering light from seeding particles (olive oil) to distinguish burnt from unburnt mixture. The seeds can reflect intense light when the diameter of the seeds in front of the flame is equal to or higher than the wavelength of the incident laser. The flame front is sharply delineated between the bright and dark areas. Then the location of the flame edge is identified from Dantec software, tracking its progression from one image to the next, using a phase boundary detection tool [46]. The detected flame edges were smoothed by a low pass filter to reduce noise from the digitization processes, and the best-fit circle to the flame edge and the related flame radius were determined using a least-squares technique. The temporal development of the flame front might therefore be used to determine the flame speed, Sn, associated with the 570 K isotherm. The adaptive PIV method was employed within the Dantec software. This is an iterative and automatic way of calculating unburnt gas velocity vectors, based on the movement of seeding particles. The shape of the interrogation area (IA) is constantly modified to accommodate the local topology of the flame front. By establishing maximum and minimum size limitations, the proper IA size was automatically established for each individual IA. The highest IA size was usually employed in the initial iteration, which was lowered in future rounds. Where the particle density was sufficiently high, this allowed for a decrease in IA sizes. The placement and magnitude of vectors were defined by the minimal IA. This point was chosen to correspond with the edge of the minimum IA. The overlap of interrogation area (IA) is often used with a typical value of 25 % for the adaptive correlation method, the IA grid is set as a maximum IA of 16×16 pixels, minimum IA of 8 × 8 pixels, and a grid step size of 2 × 2 pixels, which satisfies the requirements of hydrogen and other fuels in this study [46].

2.4. Experimental conditions

In the experiments, 99.995 % pure hydrogen was used, while 99.995 % pure methane, 99.99 % pure isooctane and n-heptane were used for comparison. The experiments employed dry laboratory air composed of O_2:N_2 in a mole ratio of 21:79 %. Measurements of the hydrogen-air mixture were made at the initial condition of 300 K, 0.1 and 0.5 MPa in spherical explosion flames over a wide range of equivalence ratios. For methane, iso-octane and n-heptane-air mixtures, obvious wrinkles occur at elevated pressures, 0.5 MPa, chosen as the initial pressure (P_i) over a range of equivalence ratios. The initial temperature (T_i) of the methane-air mixture was chosen as 300 K for comparison with the hydrogen-air mixture. For liquid fuels, $T_i = 360$ K was chosen to guarantee that iso-octane, n-heptane-air mixtures were entirely evaporated before combustion. All explosions employed the minimum ignition spark energy to ignite the mixture. For the hydrogen-air mixture, nearly 1 mJ was used for igniting all the conditions. For methane, iso-octane, and n-heptane-air mixtures, the ignition energy of about 5 mJ was used in this study.

2.5. Experimental uncertainties

Systematic uncertainties in the experimental setup encompass three primary sources of error: fuel amount (± 0.2 %), pressure measurement (± 0.05 %), and temperature measurement (± 0.7 %). Regarding the uncertainties introduced by the PIV technology, the method for measuring the combustion speed operates by recording the displacement of the flame front over a known period of time. The errors in this process are consequently related to how precisely these positions are determined in both time and space. Due to the analysis procedure and the digital nature of the recording, the position of the flame front recorded using the PIV system can only be measured to the nearest pixel position, depending on the image area and camera resolution. The flame leading edge position recorded at the isotherm where the oil particles evaporate can only be determined within a tolerance of ± 0.111 mm, based on a pixel size of 0.222 mm/pixel. Additionally, the curvature of the flame perpendicular to the laser sheet introduces a deviation in the flame position, dependent on the flame's position relative to the center of the vessel. However, since the flame front is identified with the same deviation for both moments before and after, and the flame displacement between images is small, its effect on the flame speed measurement is minimal and, in the worst case, does not exceed 0.1 mm. In each condition, the average value of the flame speed is used to minimize errors during processing.

3. Theoretical analysis

3.1. Gas velocity

In the present work, the cold front, r_u, is defined as the isotherm that is 5 K above the temperature of the reactants [25]. r_{PIV} is the temporal development of the mean flame front using PIV technique at the seeding particle evaporation isotherm (570 K for olive oil in this study). r_u is calculated based on the assumption that linear increase of temperature from unburnt gas to burnt gas:

$$r_u = r_{PIV} + \delta\left[\frac{T_P - (T_u + 5)}{T_b - (T_u + 5)}\right] \tag{3}$$

where T_P is the seeding particle evaporation temperature in PIV technique. Stretched flame speed, S_n, is derived from the cold flame radii

versus time data, $=dr_u/dt$.

Due to the difference of density across the flame front, the unburnt gas velocity u_r ranges from a minimum near the reaction zone to a maximum near the preheat zone, denoted by the term u_g, as shown in Fig. 1. Additionally, computational studies reveal a significant change in gas velocity within the flame zone, with a considerably smaller fluctuation ahead of the flame [47]. The radial unburnt gas velocity u_r can be derived from PIV measured velocity components:

$$u_r(x,y) = u(x,y)\cos(\theta) + v(x,y)\sin(\theta) \tag{4}$$

Here, $u(x,y)$ is the gas velocity component in the x-direction and $v(x,y)$ is the gas velocity component in the y-direction, $\theta = arctan\{(y-y_c)/(x-x_c)\}$. The polar transformation of the velocities begins from the determination of the global centre (x_c, y_c), as well as the point of ignition. Previous researchers have commonly employed polynomial fitting methods to determine the maximum gas velocity, typically located 0.3–1 mm ahead of the flame front in various scenarios [14–16]. However, it is important to note that PIV alone can provide accurate velocity measurements only several pixels away from the flame contour for the unburnt flow [47], and face limitations when estimating velocities very close to the flame contour. Consequently, this approach can introduce unavoidable errors. To address this limitation, a mass conservation method can be employed to derive the maximum gas velocity more reasonably. In this case, the unburnt region in the local sector is divided into a segment with a width of 2 pixel (0.444 mm), as shown in Fig. 3. The radial velocity of unburnt gas ahead of the flame front, u_r, is derived via a continuity equation in a 3D spherical coordinate:

$$u_r(r) = \frac{X}{r^2} \tag{5}$$

where $X = \frac{M}{\rho}$. $M$is a constant. More details are shown in Appendix A. As a result, unburnt gas radial velocity $u_r(r)$ is a function of r.

Fig. 4 shows instantaneous gas velocity curves for hydrogen-air mixture combustion at P_i = 0.1 MPa, T_i = 300 K with zero distance indicating the evaporation isotherm. Three cases are chosen to be presented in this study, $\phi = 0.8$ at $t = 2.0$ ms after ignition, $\phi = 1$ at $t = 1.5$ ms after ignition, $\phi = 1.2$ at $t = 1$ ms after ignition, respectively. For accuracy, the distance of about 3 mm near the cold flame front is used to fit Eq. (5) to extrapolate unburnt gas radial velocity at flame contour $u_r(R_i)$, producing the value of R^2 of 0.9:

$$u_r(r) = \frac{X}{r^2} = \begin{cases} \dfrac{9200}{(D_R+31.2)^2}, & t = 2\ ms(\phi = 0.8) \\ \dfrac{16200}{(D_R+32.2)^2}, & t = 1.5\ ms(\phi = 1.0) \\ \dfrac{8800}{(D_R+22.8)^2}, & t = 1.0\ ms(\phi = 1.2) \end{cases} \tag{6}$$

D_R is the gas radial distance ahead of the 570 K olive oil evaporation isotherm, 31.2, 32.2, 22.8 mm are the temporal PIV mean flame fronts for three conditions. In addition, X (= 9200, 16,200, 8800), $r = (D_R + 31.2$ m $D_R + 32.2$, $D_R + 22.8)$ are only applicable for the particular time instant and segment for these three specific conditions. The remaining data are same as the three presented in Fig. 4. In order to form a representative unburnt gas radial velocity, a certain amount of velocity samples u_g in the local segment in one annulus are needed for averaging, then the mean gas velocity at the cold flame front location (r_u) using continuity conservation, u_{gc}, is achieved. The maximum mean gas velocity using 6th polynomial fitting method, u_{gp}, is also derived and obtained for the purpose of comparison, as shown in Fig. 4. u_{gc} is slightly higher than u_{gp} all the time. As mentioned before, the accuracy of fresh gas velocity adjacent to the flame front is a PIV limitation that makes it difficult to accurately estimate the velocity vectors inside the narrow region in front of the flame. Additionally, it has been demonstrated that the velocity magnitude just ahead of the artificial dark region is reduced compared with the original and real one [47]. Consequently, the unburnt gas velocity using continuity conservation, u_{gc} is more

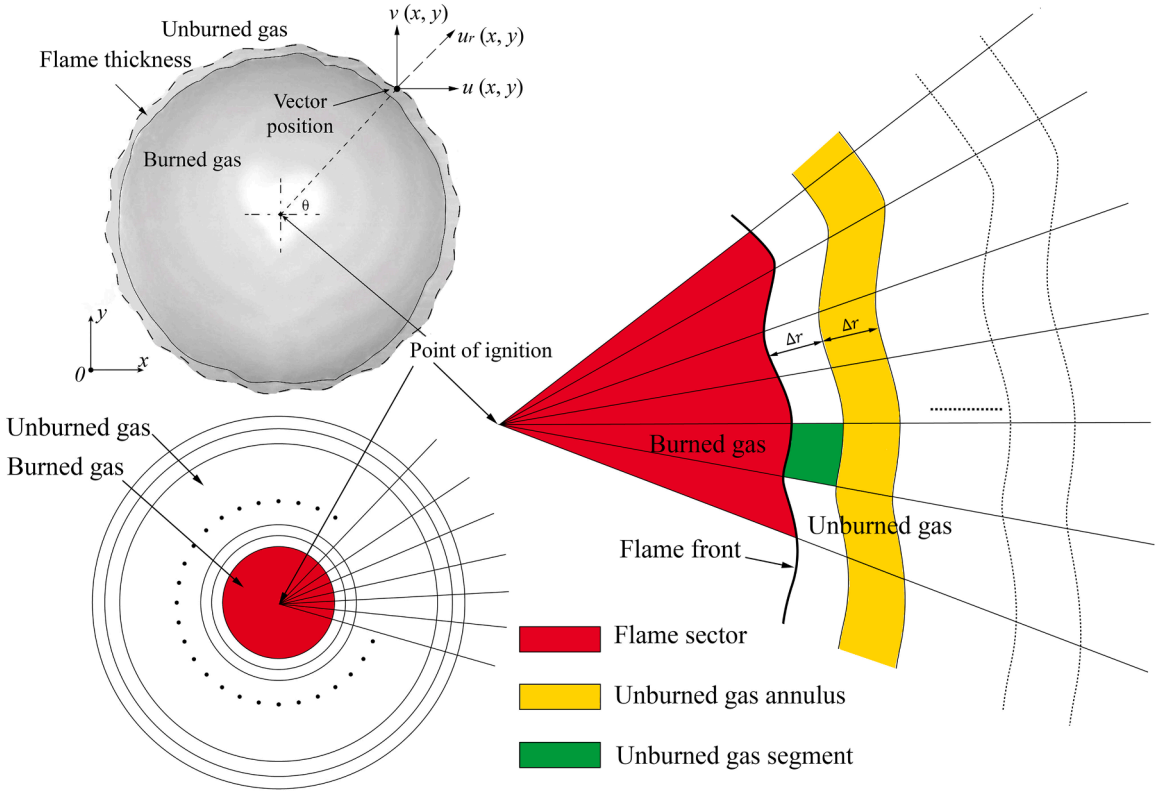

Fig. 3. Schematic diagram of gas vector measurements for hydrogen-air mixture at the laminar unstable regime.

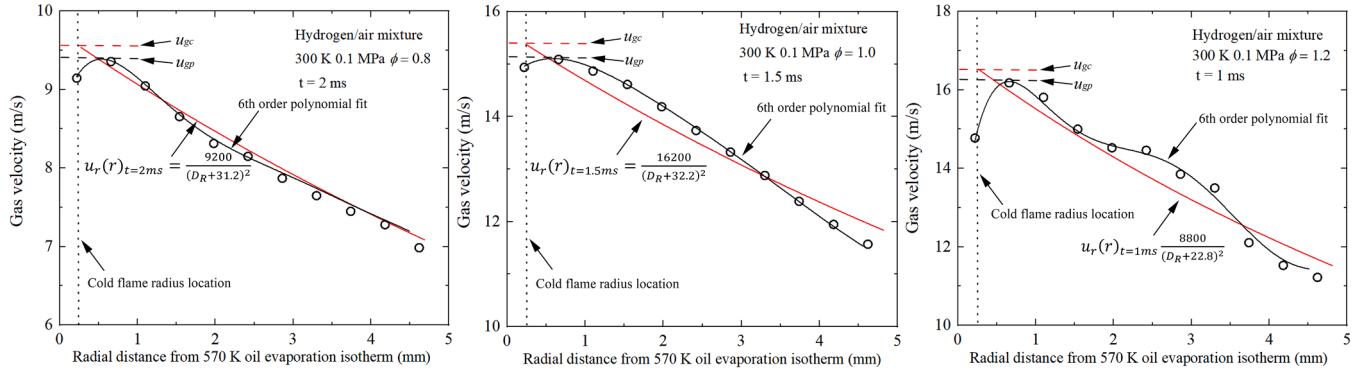

Fig. 4. Profile of the fresh gas velocity in one annulus for hydrogen-air mixture of $P_i = 0.1$ MPa, $T_i = 300$ K, $\phi = 0.8, 1.0, 1.2$.

scientifically reasonable than the maximum gas velocity using a traditional polynomial fitting method, u_{gp}.

3.2. Stability limits

The unstable flame is accompanied by a cellular spectrum encompassing a range of perturbing wavelengths with defined upper and lower limits, denoted as cutoffs ($\Lambda_{min} < \Lambda < \Lambda_{max}$), as described by linear stability theory [12]. Disturbances characterized by wavelengths exceeding the maximum wavelength (Λ_{max}) (approximately equal to the flame radius) are mitigated by the flame stretch mechanism. Conversely, disturbances with wavelengths shorter than the minimum wavelength (Λ_{min}) are stabilized by diffusion effects. According to stability analysis as presented in [48], the wavelength corresponding to the smallest cell size converges to a constant value as the flame expands, resulting in the disappearance of cells with smaller sizes. Empirical evidence supporting these stabilization mechanisms is provided in experiments [7], justifying the use of Λ_{min} as the mean cell size for fully developed cellular flames. Further quantitative details and results are available in [2,12]. The calculation of the minimum wavelength is derived as follows: $\Lambda_{min} = 2\pi r n_{max}$, where n represents a wavenumber. Additionally, Peclet number (Pe), given by r/δ, exhibits a linear relationship with n_{max}. By setting $Pe/n_{max} = \Gamma$, it can be deduced that $\Lambda_{min} = 2\pi r/n_{max} = 2\pi\delta\Gamma$. In essence, Γ can also serve as a representation of the mean cell size normalized by $2\pi\delta$, a value accessible from [2].

3.3. Flame thickness

It is necessary to consider the laminar flame thickness, δ, which is defined as the distance between the burnt zone and unburnt zone, in this study [1]. Additionally, flame thickness is the prerequisite parameter of some dimensionless numbers in this study (Markstein number, Karlovitz number, etc.). The laminar planar flame thickness using is based on the temperature profile derived from 1-D spherical flame code:

$$\delta = (T_b - T_u)/(dT/dx)_{max} \tag{7}$$

where $(dT/dx)_{max}$ is the maximum temperature gradient. Then the simulated flame thicknesses are plotted against the time at various equivalence ratios (Fig. 5 (a)) and flame stretch rates (Fig. 5 (b)). The flame stretch rate, α_f, of a spherical explosion flame is given by: $\alpha_f = \frac{2}{r_u} S_n$ [1]. As time passes after ignition, flame thickness in Fig. 5 (a) increases and reaches a peak, which may be due to the effect of ignition energy. After that it levels off to a nearly constant value. The 2nd order polynomial fittings are used to get the unstretched flame thickness with $R^2 > 0.95$, as shown in Fig. 5 (b) with dotted lines, which is consistent with results [1] using Chemkin-Pro 19.1 software with the GRI 3.0 combustion kinetics. Consequently, this methodology is used in this study for all situations.

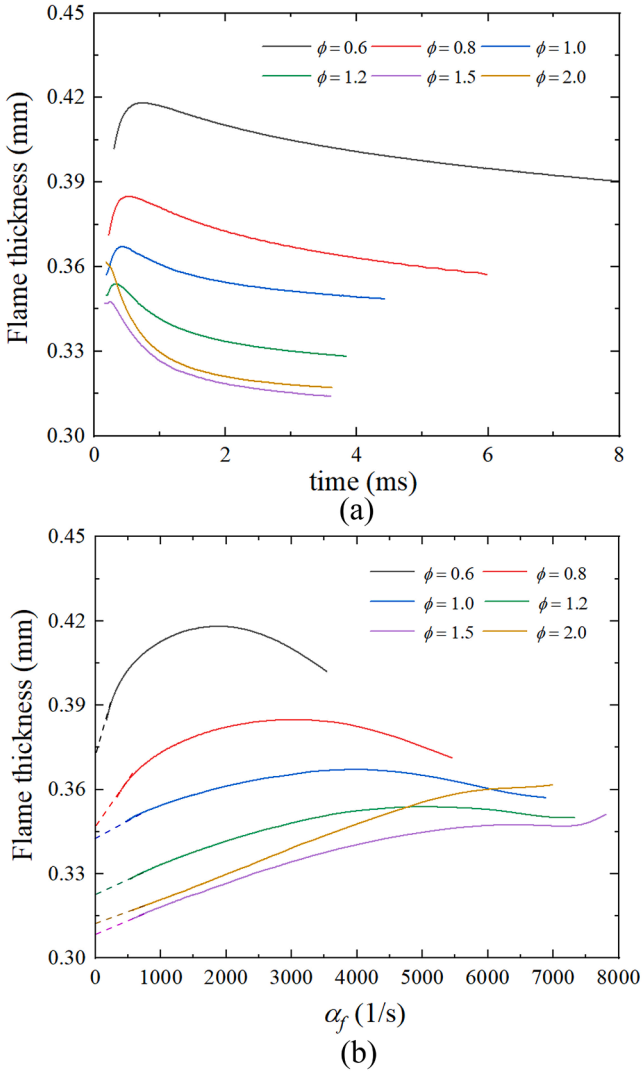

Fig. 5. (a) the time history of predicted flame thickness for hydrogen-air flames at $P_i = 0.1$ MPa and $T_i = 300$ K, $\phi = 0.6$–2.0. (b) the same flame thickness as a function of stretch rate.

3.4. Dimensionless numbers

Various parameters are linked to the occurrence of flame instabilities. A key parameter is the critical flame radius, r_{cl}, the flame radius at which the cellular flame structure becomes apparent and flame

speed surges spontaneously [1]. Correspondingly, since the flame is stabilised by the stretch, the dimensionless parameter K_{cl} ($\alpha_{cl}\frac{\delta}{u_l}$) expressed on the critical total flame stretch rate, is a more relevant parameter to represent the onset of instability [21], where α_{cl} is α_f at the critical radius. The Lewis number (Le), defined as the ratio of the thermal diffusivity of the mixture to the mass diffusivity in the inert mixture of reactants, and reflects the intensity of thermal diffusion instability of the cellularly unstable hydrogen-air flames. Considering the combined effect of the Lewis number of the fuel and oxidizer, the effective Lewis number (Le_{eff}) is used [48]:

$$Le_{eff} = 1 + \frac{(Le_E - 1) + (Le_D - 1)\mathscr{A}}{1 + \mathscr{A}} \tag{8}$$

where Le_E is Lewis number of excessive reactants, Le_D is Lewis number of deficient reactants. $\mathscr{A} = 1 + Ze(\Phi - 1)$ is a measure of the strength of the mixture. The Φ is defined as the ratio of the mass of excess to deficient reactants in the fresh mixture relative to their stoichiometric ratio. In other word, $\Phi = \phi$ for fuel rich mixtures, and $\Phi = 1/\phi$ for fuel lean mixtures. Here, $Ze = E_a(T_b - T_u)/(R^0 {T_b}^2)$ is the Zeldovich number, E_a, the activation energy, and R^o, the universal gas constant.

The theoretical expression of Markstein number Ma is proposed by [49]:

$$Ma = \frac{\sigma}{\sigma - 1}\ln\sigma + \frac{Ze(Le - 1)}{2(\sigma - 1)}\int_0^{\sigma - 1}\frac{\ln(1 + x)}{x}dx \tag{9}$$

The presence of Darrieus-Landau (DL) instability is attributed to the density discontinuity across the flame thickness, making the density ratio σa relevant factor in hydrodynamic instability. In addition, Lewis number is a key component in Eq. (9) for Markstein number. Therefore, Markstein number accounts for both thermal diffusion and hydrodynamic effects.

4. Results and discussions

4.1. Flame speed and unburnt gas velocities

Fig. 6 displays the variations of both the measured experimental flame speed and simulated flame speed calculated using a 1D spherical flame code [23] with detailed kinetic schemes [24], as a function of flame radius (r_u), for explosions at ϕ of 0.8, 1.0, and 1.2, temperature of 300 K, and pressure of 0.1 MPa. Meanwhile, Fig. 7 illustrates the comparisons between the measured experimental gas velocities (u_{gc}), calculated using the continuity equation, and the simulated gas velocities (u_{gs}) derived from the 1D spherical flame model [23] that was selected at the mean cold flame front location (r_u). The experimental and simulated outcomes exhibit a degree of proximity and demonstrate a noteworthy level of consistency. Unburnt gas velocities adjacent to the flame front, u_{gc} (continuity equation method), u_{gp} (6th polynomial fitting method) and u_{gs} at r_u = 30 mm are presented in Fig. 8 for stable hydrogen-air mixtures at, ϕ = 0.4–2.0, P_i = 0.1 MPa and T_i = 300 K. The u_{gc} is slightly higher than u_{gp} for most equivalence ratios. The simulated gas velocities are slightly lower than the experimental data derived u_{gc} and u_{gp}, which can be attributed to that some variables such as heat loss, radiation and wall confinement of the combustion chamber may lead to discrepancies between the experimental and simulated gas velocities.

4.2. Self-acceleration regime

During the expansion of the laminar flame, two distinct instances featuring irregular flame surfaces were observed. Firstly, there was a continuous development of substantial cracks along with their branches. Secondly, there was a sudden and spontaneous emergence of numerous cellular structures encompassing the entire flame surface. Notably, the characteristic dimensions of these cells were considerably smaller compared to the larger cracks. This phenomenon is attributed to hydrodynamic instability. In summary, the second instance is deemed as the initiation of flame instability in this investigation [1]. Moreover, the abrupt and spontaneous appearance of these cellular structures across the entirety of the flame surface coincides with a rapid increase in flame propagation speed [22]. Therefore, in a PIV measurement, a steep rise in flame speed or gas velocity profile due to wrinkled flame surface is used as an indicator for the starting point of a laminar unstable regime [22]. Fig. 9 depicts the fluctuations of u_{gc} concerning flame radius r_u across hydrogen-air mixtures. Notably, an upsurge in u_{gc} is observed subsequent to the onset of instability. Furthermore, it is observed that the initiation of instability appears to transpire at larger flame radii as ϕ escalates.

An in-depth analysis of the flame propagation acceleration process entails a comprehensive investigation into flame speed, gas velocity adjacent to the flame front, and their mutual interrelation. The flame speed and gas velocity are plotted against time in Fig. 10, and it can be found that they both exhibit an accelerated behaviour accompanied by pulsation after the onset of instability. As the cell over the flame surface expands, it becomes unstable due to a decrease in the localized stretch rate on its surface. This instability prompts the cell to divide into smaller cells with higher localized stretch rates, facilitating its stabilization. This process of fissioning into smaller cells with varying acceleration rates continues, resulting in a cyclical pattern of faster and slower acceleration stages. Throughout this cycle of strong and weak acceleration phases, the unstable flame exhibits a global pulsing acceleration pattern at a specific frequency [2]. Therefore, in analogous to Eq. (2) for the flame speed, the unburnt gas velocities adjacent to the flame front, u_{gc} can be written as follows:

$$u_{gc} = A_g\alpha_g t^{\alpha_g - 1} + B_g\sin\left(2\pi f_g t + \lambda_g\right) \tag{10}$$

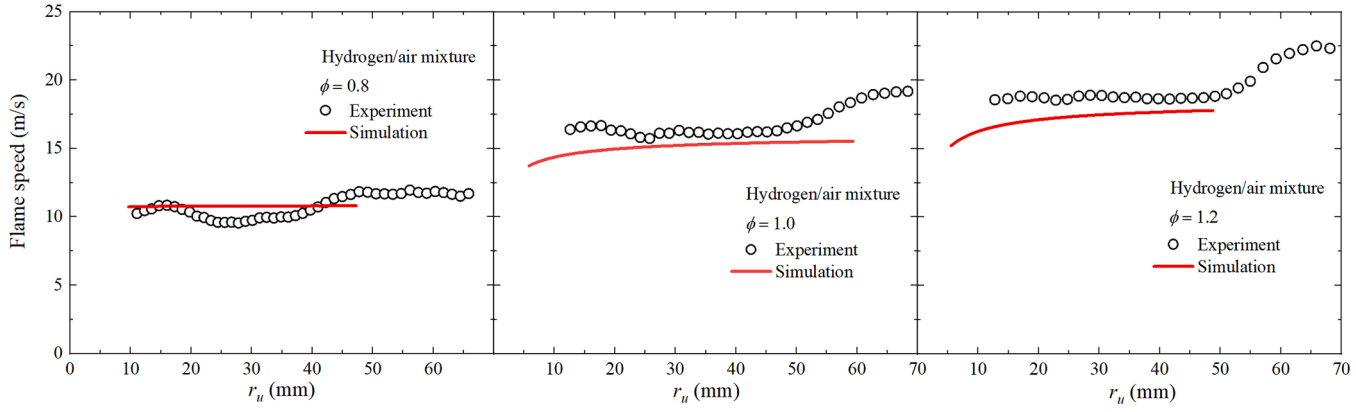

Fig. 6. Variations of flame speed against the flame radius of hydrogen-air mixtures at P_i = 0.1 MPa and T_i = 300 K.

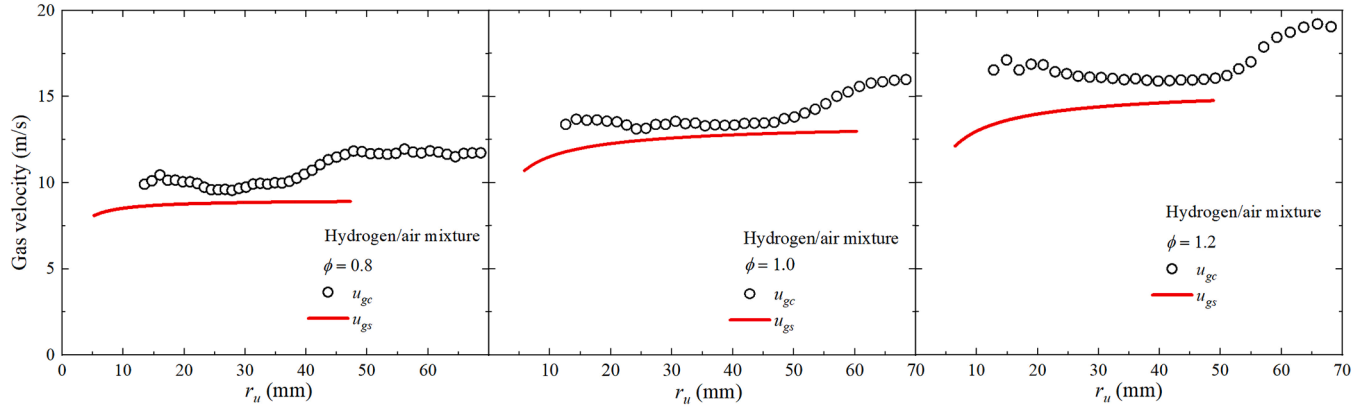

Fig. 7. Variations of gas velocities against the flame radius of hydrogen-air mixtures at $P_i = 0.1$ MPa and $T_i = 300$ K.

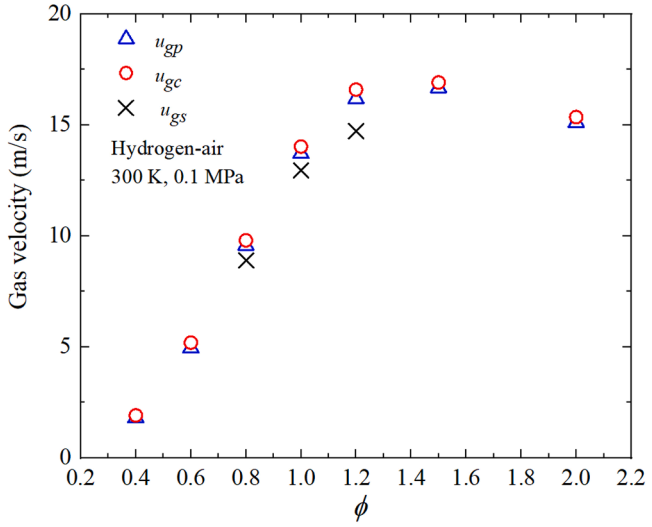

Fig. 8. Variations of u_{gp}, u_{gc}, u_{gs} of stable hydrogen-air mixtures at $P_i = 0.1$ MPa and $T_i = 300$ K plotted against ϕ from 0.4 to 2.0.

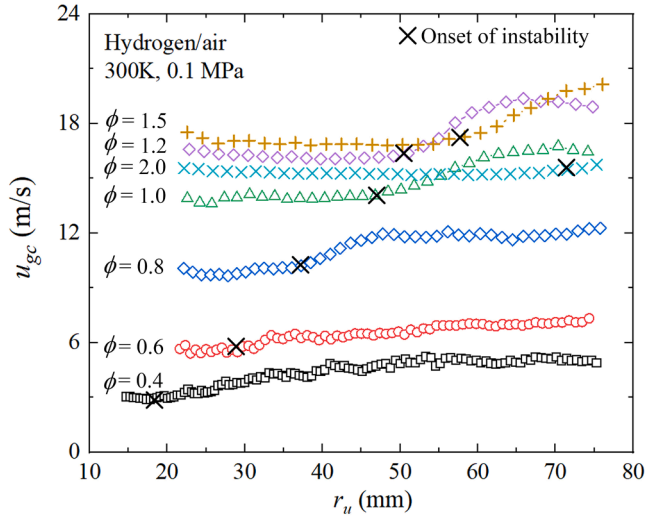

Fig. 9. Variations of u_{gc} with r_u, for hydrogen-air mixtures at $P_i = 0.1$ MPa, $T_i = 300$ K and $\phi = 0.4 - 2.0$. Cross symbols signify the onset of instability.

where A_g is the empirical constant for u_{gc}, α_g is the acceleration exponent for u_{gc}. $f_g$is frequency for u_{gc} (s^{-1}), B_g is the amplitude for u_{gc} (m/s) and λ_g is phase difference for u_{gc}. The experimental acceleration exponents, α and α_g can be extracted by the time history of S_n and u_{gc}, shown in Fig. 10. Moreover, the extracted acceleration exponent α and α_g are plotted against ϕ in Fig. 11. The results of the investigation demonstrate a close proximity between α and α_g, signifying their mutual interaction in the self-acceleration of S_n and u_{gc}. For hydrogen-air blends, the values of exponents α and α_g lie between 1.18 to 1.31 under the current condition, whereas for methane, iso-octane, and n-heptane mixtures, these fluctuations range from 1.13 to 1.28, 1.12 to 1.36, and 1.11 to 1.41 at $P_i = 0.5$ MPa, respectively.

4.3. Self-disturbance regime

The gas velocity vector maps of hydrogen-air combustion are shown in Fig. 12, with the magnitude of the velocity vectors coloured in. The elapsed time after the ignition is labelled for each vector map. The flame surface remains smooth at the early stage of propagation ($t = 1$ ms) and then the cellular structure over the flame surface appears ($t = 2.6$ ms, not shown in Fig. 12), indicating the onset of instability. At $t = 1$ and 2.2 ms, the vectors with nearly the same magnitude are evenly distributed within the unburnt gas annulus around the flame front. As time progresses (at t = 3.0, 3.5 and 4.3 ms), the flame front experiences increasing expansion with a correspondingly decreasing stretch rate, causing it to destroy stable flame surface and develop wrinkles induced by flame instabilities due to the low stretch effects. This further causes the velocity vectors near the flame front to fluctuate more and gas flow direction anisotropically. A zoom-in image showing the detailed velocity vector for a quarter flame is presented in Fig. 12 (b). The evolution of a disturbed spherical flame front seems to induce different levels of perturbations and the subsequent flow domain. When the flow adjacent to a cellularly unstable flame front becomes disturbing, it is called self-turbulization previously [3]. The gas flow disturbed by the flame front is consumed by the propagating flame front before it is convected to the far field. As shown in Fig. 12 (b), the RMS gas flow velocity decreases monotonously with the radial direction away from the flame surface.

Based on Figs. 4 and 12, it can be observed that the gas velocity in the proximity of the flame front decreases monotonically with radius as the effect of flame propagation weakens away from the flame front. These results suggest that the flow structures generated by the flame are primarily restricted to the vicinity of the flame front. Liu et al. [3] reported $u_t^2 \sim \nabla g \cdot \nabla g$, where u_t is gas flow velocity in the tangential direction, g is the fluctuation of the flame front from the mean surface for a mildly wrinkled one. This reveals that fluctuations or wrinkles of the flame front induce the tangential gas flow velocities, and then further 'turbulence' or disturbance. Therefore, to further understand relationship

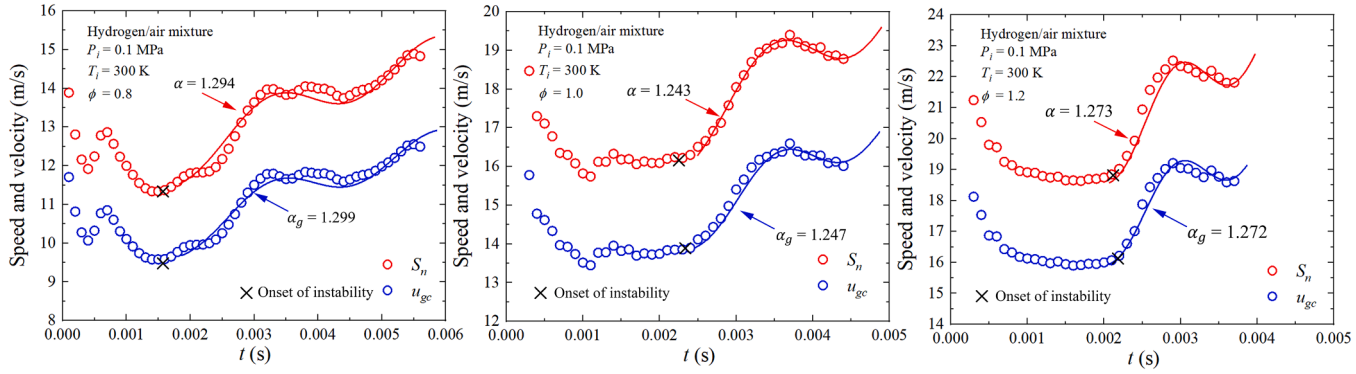

Fig. 10. Propagation flame speed S_n and u_{gc} against time for hydrogen-air combustion at $P_i = 0.1$ MPa and $T_i = 300$ K and $\phi = 0.8$, 1.0, 1.2. Cross symbols signify the onset of instability. The solid lines are determined based on Eqs. (2)&10.

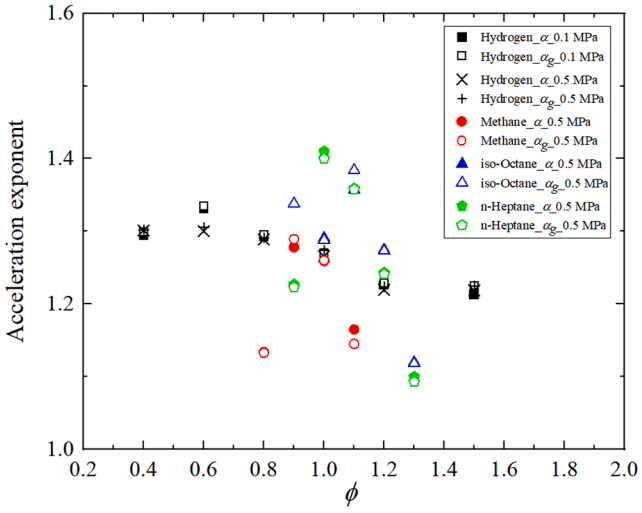

Fig. 11. Experimentally extracted acceleration exponents, α and α_g, for hydrogen-air mixture at $P_i = 0.1$ and 0.5 MPa and $T_i = 300$ K, methane-air mixture at $P_i = 0.5$ MPa and $T_i = 300$ K, isooctane-air mixture at $P_i = 0.5$ MPa and $T_i = 360$ K, n-heptane-air mixture at $P_i = 0.5$ MPa and $T_i = 360$ K.

between gas flow disturbance after instability and the wrinkled flame surface, the power spectral density (PSD) of flame surface wrinkling and disturbed flow field ahead of the flame front needs to be analysed and compared. PSD was derived by the Fourier transform of wrinkling amplitudes (g) and gas velocities (u_{gc}) at a wave number k ($k = 2\pi/L$). The wavelength of wrinkled flame (L) roughly ranges from flame radius (maximum length scale) to the flame thickness (smallest scale)~pixel size. The Power Spectral Density (PSD) analysis of gas velocities adjacent to the flame front ($S_g(k)$) and PSD of wrinkling amplitudes of the flame front ($S_f(k)$) both show a power-law dependence with wavenumber in the form of $k^{-2.7}$ roughly. This indicates that the fluctuations or wrinkles of the flame front may induce the gas flow velocities, then the study proceeds to evaluate the theoretical approximation of β in the scaling of $S_g(k) \sim S_f(k) \sim k^{-\beta}$, based on the fractal attribute typical of the cellularly unstable laminar flame fronts. As previously discussed in Refs. [12–14], the hydrodynamically unstable flame tends to exhibit fractal characteristics, while the diffusive-thermally unstable flame typically does not. It is reasonable to assume the experimentally measured fractal dimension ($D = 1 + d \approx 1.19 \sim 1.29$) in the hydrogen-air flames mainly contributed to flame instability. Consequently, we can infer that the value of β, which relates to the fractal dimension through $D = \beta/2$, should fall within the range of 2.38 to 2.58 in this study. This estimation broadly corresponds to the observed value of 2.7 for β. This alignment reinforces the conclusion from Liu et al. [3] that the fractal dimension of the flame edge is represented by $D = \beta/2$. The PSD of gas velocities and flame wrinkling have a steeper slope (−2.7) than that for isotropic turbulence within the inertial sub-range in which the energy spectra exhibit $a - 5/3$ decay measured from the bomb [44]. This observation suggests that the gas flow preceding the flame front may not be strictly characterized as turbulent flow. Consequently, there is a compelling need for an in-depth investigation and quantification of the gas fluctuations occurring ahead of the flame front.

The subsequent study is then centred on the quantification of the strength of the gas flow disturbance close to the wrinkled flame front since it was known that the majority of the flame-generated flow structures were restricted in the area around the flame front. Therefore, the spatial RMS velocity around the flame surface front (u'_{gc}) was calculated in one annulus within the prescribed zone (0.444 mm) of preheating and reaction around the flame front:

$$u'_{gc} = \sqrt{\left(\frac{1}{N_p}\sum_{p=1}^{N_p}\left(u_g - u_{gc}\right)^2\right)} \tag{11}$$

where u_{gc} is the mean gas velocity in one annulus, N_p is the total number of velocity vectors in the annulus. It is presented as a function of hydrogen-air flame cold front radius in Fig. 13. Initially, u'_{gc} remains relatively stable across all equivalence ratios until the onset of instability. Subsequently, it undergoes an increase and exhibits oscillatory behaviour around a low approximately constant value around 0.2 to 0.5 m/s. For the sake of generality, the gas flow disturbance intensity denoted as $\overline{u'_{gc}/u_{gc}}$, is introduced as an assessment parameter to quantitatively measure the intensity of disturbances induced by instability:

$$\overline{u'_{gc}/u_{gc}} = \frac{\sum_{r_{cl}}^{r_{max}}\left(u'_{gc}/u_{gc}\right)}{N_r} \tag{12}$$

Here N_r represents the total number of velocity points within the specified range of radii, $\overline{u'_{gc}/u_{gc}}$ represents the average value of u'_{gc}/u_{gc} within the range extending from r_{cl} to r_{max}. r_{max} denotes the maximum observable radius.

Fig. 14 shows variations of $\overline{u'_{gc}/u_{gc}}$ against ϕ of hydrogen-air mixture at $P_i = 0.1$ and 0.5 MPa, respectively. The increase in $\overline{u'_{gc}/u_{gc}}$ with decreasing ϕ can be explained by the reduction of Le_{eff}. This results in mass diffusive fluxes becoming dominant over heat fluxes, which in turn is indicative of an unstable flame. Furthermore, as previously discussed, the degree of DL instability indicated by the extensively corrugated flame front becomes more pronounced with increasing pressure. Consequently, this phenomenon leads to an elevation of gas flow disturbance intensity, which signifies higher gas velocity disturbances. Augmented pressure levels prompt a decrease in flame thickness, which

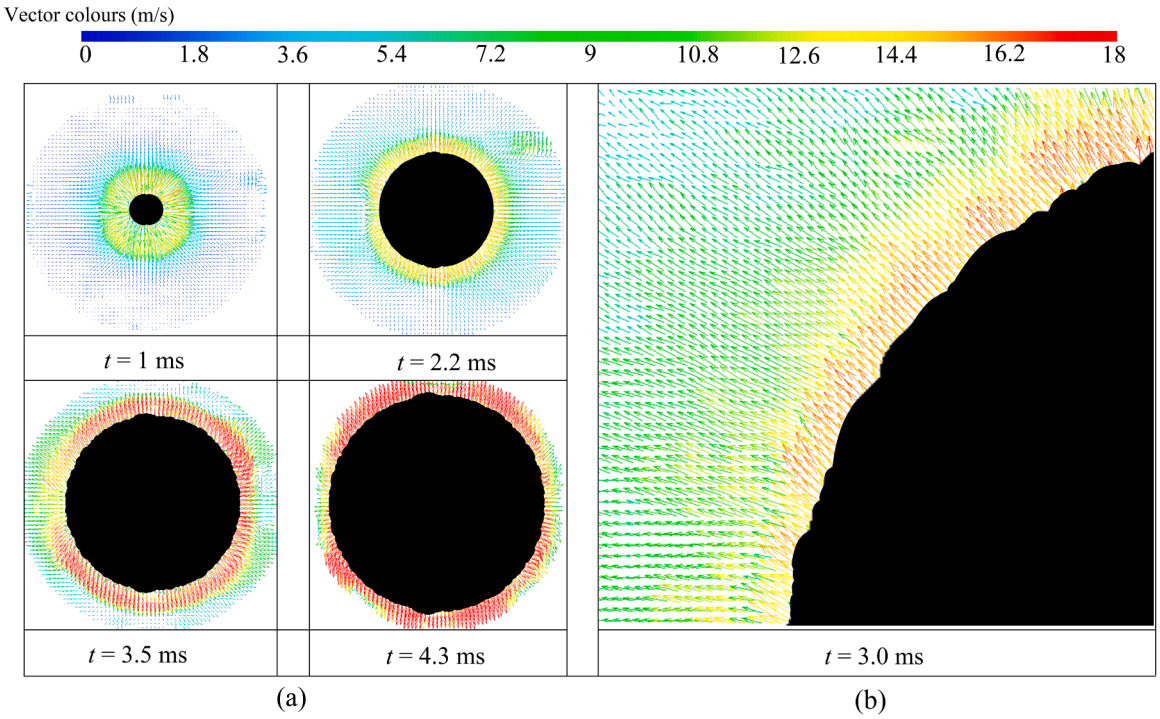

Fig. 12. Vector maps of hydrogen-air laminar flames at ϕ =1.0, P_i = 0.1 MPa and T_i = 300 K. Black solid circles represent the burnt gas. (a) global gas vectors of the evolution of flame expansion from t = 1 to 4.3 ms; (b) detailed gas vectors at the top left corner of flame expansion at t = 3.0 ms.

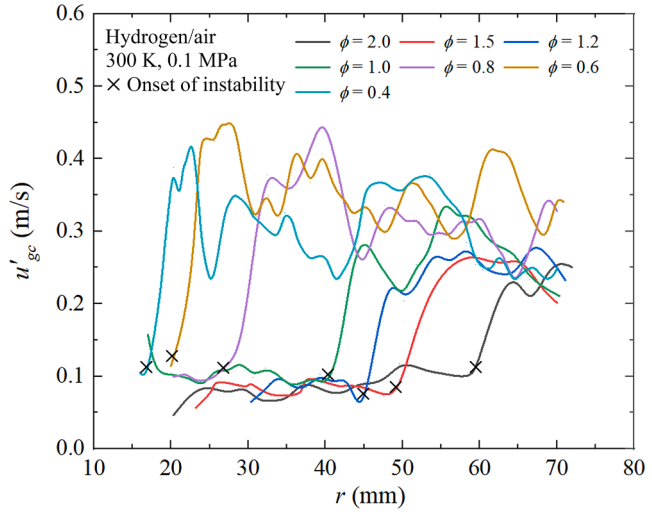

Fig. 13. Variations of $u_{gc}^{'}$ against the flame cold front radius for hydrogen-air mixtures at T_i = 300 K and P_i = 0.1 MPa. Cross symbols signify the onset of instability.

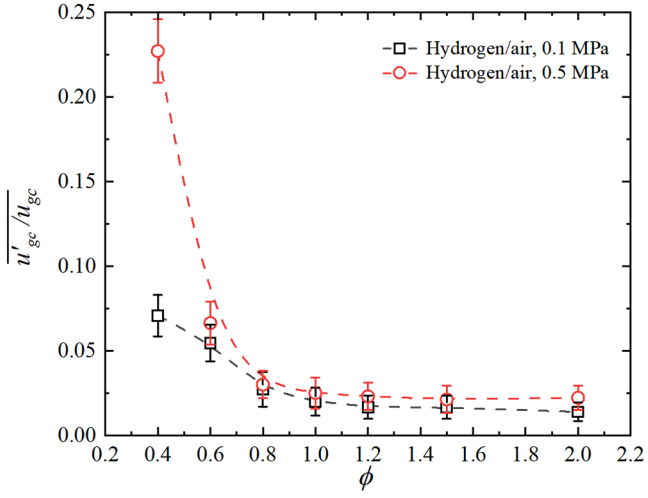

Fig. 14. Variations of $\overline{u_{gc}^{'}/u_{gc}}$ against ϕ for hydrogen-air mixtures at T_i = 300 K and P_i = 0.1 and 0.5 MPa. Error bands are for experiments.

renders the flame more susceptible to flow-induced disturbances.

Based on 2D Mie-scattering image, the perimeter of the 2D wrinkled flame is calculated in MATLAB using 'bwperim' and 'length' functions and then equating it to the perimeter of an equivalent circle as $P_T = 2\pi R_T$, allowing for the calculation of R_T. Subsequently, the 3D total surface area of the wrinkled flame is computed using the formula $A_T = 4\pi R_T^2$, as described in Ref. [50]. Following that, $A_L = 4\pi r_u^2$ is used to get the matching mean spherical flame surface area. The wrinkling factor (A_T /A_L) experiences an increase with an escalation in pressure (stronger DL instability due to thinner flame thickness) and a decrease in equivalence ratio (variations of competition between thermal diffusivity and mass diffusivity). The wrinkling factor (A_T /A_L) at very lean and rich conditions is plotted against ϕ in Fig. 15. The larger A_T /A_L happens in the leaner mixture with higher pressure. Additionally, following the flame instability, A_T /A_L rise gradually for a while, and then increases at a faster pace with the further expansion of spherical hydrogen-air flame.

The gas flow disturbance intensity ($\overline{u_{gc}^{'}/u_{gc}}$) due to the wrinkled flame surface (A_T /A_L) at r_u = 65 mm is plotted in Fig. 16. It is clear that a more wrinkled flame surface (greater A_T /A_L) results in higher gas flow disturbance intensity ($\overline{u_{gc}^{'}/u_{gc}}$). This supports the PSD analysis, indicating that the initial smooth flame surface becomes wrinkled due to flame instabilities, which further intensify the disturbance of the neighboring flow. Then the induced disturbance and increasing flame surface area both increase the flame propagation speed.

It is evident that a flame surface exhibiting greater wrinkling (indi-

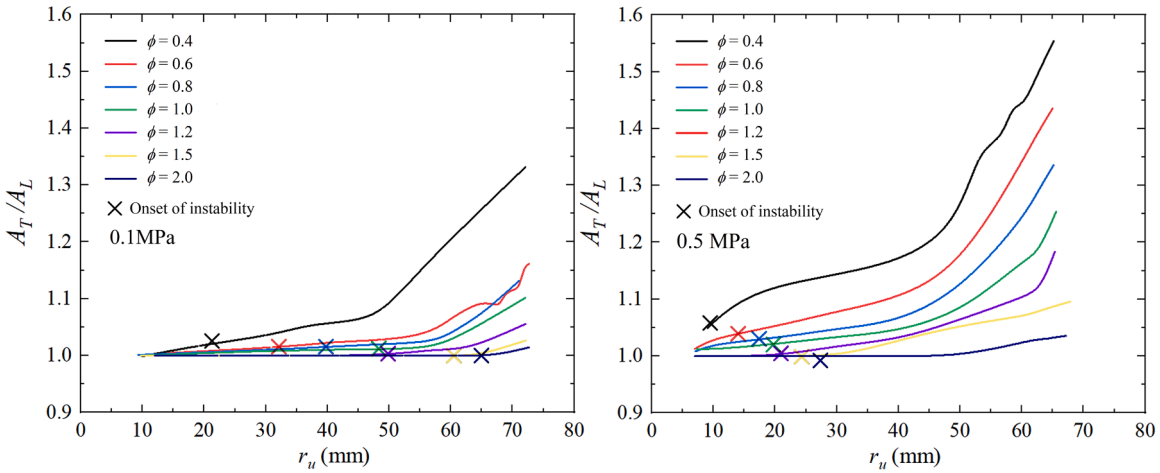

Fig. 15. Evaluated wrinkling factor A_T/A_L of hydrogen-air mixture against ϕ at 300 K.

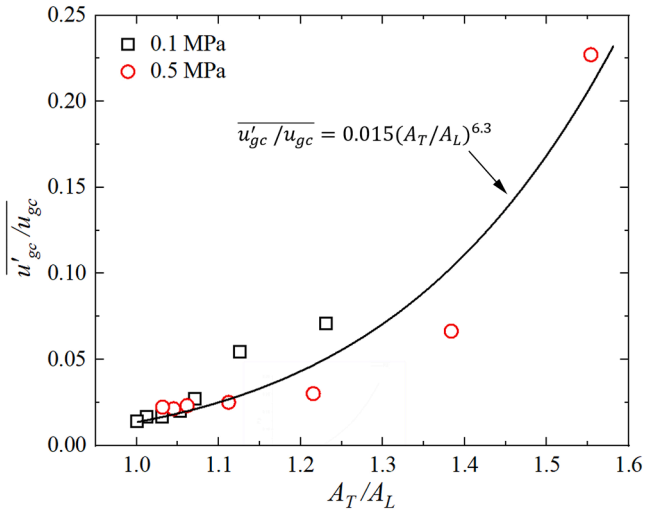

Fig. 16. Evaluated $\overline{u'_{gc}/u_{gc}}$ against wrinkling factor A_T/A_L of hydrogen-air mixture at 0.1 and 0.5 MPa. The solid black line is the fit line for all the points.

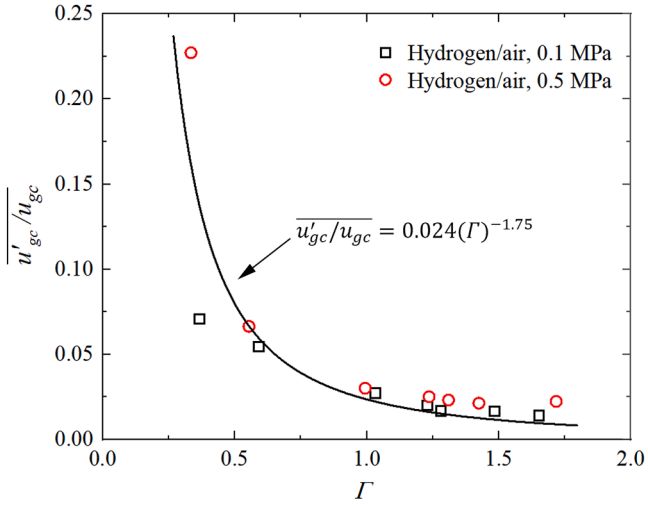

Fig. 17. Evaluated $\overline{u'_{gc}/u_{gc}}$ against normalized mean cell size Γ of the hydrogen-air mixture. The solid black line is the fit line for all the points.

cated by a higher A_T/A_L ratio) corresponds to a heightened gas flow disturbance intensity ($\overline{u'_{gc}/u_{gc}}$). This observation aligns with the findings of the Power Spectral Density (PSD) analysis, suggesting that the initial smooth flame surface undergoes wrinkling due to flame instabilities. This, in turn, enhances disturbances in the adjacent flow. Consequently, the induced disturbances, coupled with the expansion of the flame surface area, collectively contribute to the increase in flame propagation speed. Moreover, a solid black fitting parabola was used to fit all the points:

$$\overline{u'_{gc}/u_{gc}} = 0.015(A_T/A_L)^{6.3} \tag{13}$$

The continuous generation and development of cells across the flame surface theoretically contribute to gas flow disturbances and potential vorticity. However, these effects might not be fully resolved with current experimental techniques ahead of the flame surface. In Fig. 17, the relationship between gas flow disturbance intensity and theoretically calculated normalized mean cell size is presented. The graph shows that smaller mean cell sizes correspond to higher gas flow disturbance intensities. These unstable manifestations of flame surfaces adorned with characteristic-sized cells are not only captivating but also appear to be the source of the gas fluctuations observed ahead of the flame front. A solid black parabolic curve was used to fit all the data points.

$$\overline{u'_{gc}/u_{gc}} = 0.024(\Gamma)^{-1.75} \tag{14}$$

Given the known relationship between the power-law exponent of the PSD of gas velocities ahead of the flame front and the fractal dimension of the flame edge, it is valuable to investigate the direct relationship between the self-acceleration (acceleration exponent, α) and self-disturbance (gas flow disturbance intensity, $\overline{u'_{gc}/u_{gc}}$). It has been demonstrated in the previous sections that a wrinkled flame surface would result in flame acceleration, and more wrinkled flame surfaces with smaller cell sizes would result in stronger gas flow disturbances. The linear increasing relationship between the disturbance strength of gas velocities and higher acceleration exponents, as observed in Fig. 18, appears to be quite weak. This suggests that there is no obvious causal link between self-acceleration and self-disturbance. Both phenomena are attributed to the wrinkled flame surface.

The empirical correlations for $\overline{u'_{gc}/u_{gc}}$ are sought in terms of laminar critical Karlovitz number (K_{cl}), effective Lewis number (Le_{eff}) and burnt gas Markstein number (Ma_b). Burnt gas Markstein number (Ma_b) is a ratio of the Markstein lengths L_b [1] to flame thickness obtained by 1D spherical flame code [23] with detailed kinetic schemes [24]. From a

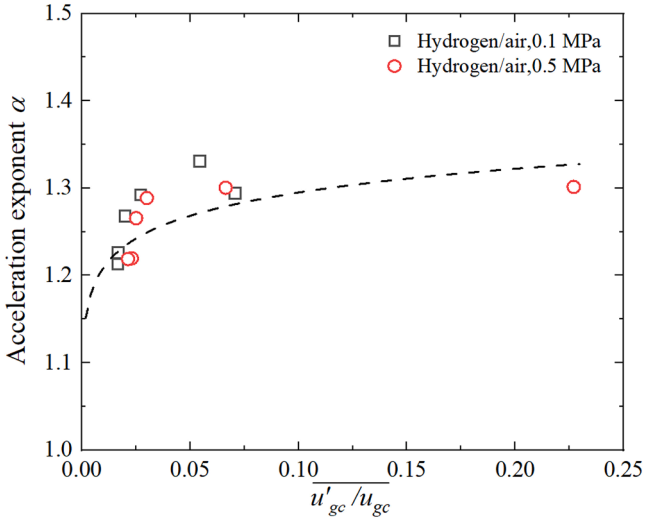

Fig. 18. Variations between $\overline{u'_{gc}}/u_{gc}$ and α.

dimensionless perspective, the correlation between $\overline{u'_{gc}}/u_{gc}$ and K_{cl} is helpful in understanding the link between intrinsic disturbance intensity and the onset of instability; the correlation between $\overline{u'_{gc}}/u_{gc}$ and Le_{eff} is for intrinsic disturbance intensity and thermal diffusion effects (competitiveness between simultaneous heat and mass transfer); the correlation between $\overline{u'_{gc}}/u_{gc}$ and Ma_b is for intrinsic disturbance intensity and strength of stretch. A substantial positive association between $\overline{u'_{gc}}/u_{gc}$ and K_{cl} is discovered, as shown in Fig. 19 (a). K_{cl} can be deducted as the following equation: $[2(\rho_u/\rho_b)/Pe_{cl}]/[1+(2Ma_b/Pe_{cl})]$ [1], where Pe_{cl} is r_{cl}/δ, a higher value of K_{cl} indicates an earlier onset of instability. Moreover, the extent of instability progressively intensifies as it occurs at an earlier stage.

As depicted in Fig. 19 (b), $\overline{u'_{gc}}/u_{gc}$ shows a decrease with an increase in Le_{eff}. When Le_{eff} is less than unity, mass diffusive fluxes prevail over heat fluxes, indicating an unstable flame. It can be explained by the fact that more energy congregates at the zenith of the flame front, thereby raising local burning velocity, yet diverging gas flow brings about an opposite influence at the crest, which causes a reduction in both burning velocity and local temperature. Consequently, the distortion of the flame enlarges, rendering it increasingly unstable. However, for Le_{eff} greater than unity, thermal diffusion mechanisms counterbalance the hydrodynamic instability, leading to a reduced burning velocity at the apex of the flame front, stabilising the flame. Similarly, the increase in Ma_b induces a parabolic decrease of $\overline{u'_{gc}}/u_{gc}$. Fig. 19 (c) also indicates that strong stretch smoothens the flame surface and weakens disturbance intensity, which constitutes an equally crucial observation. Under the specific conditions characterized by a high critical Karlovitz number, low effective Lewis number, and high negative burned gas Markstein number, it is noteworthy that gas flow disturbance intensity exhibits a greater magnitude at 0.5 MPa compared to 0.1 MPa. This observation suggests that, under elevated pressure conditions, the intensity of gas flow disturbances is more significantly influenced and sensitively responsive to these dimensionless parameters. The different methods of calculating flame thickness can result in variations in the quantification of these dimensionless parameters. Therefore, these figures provide a rough idea of the relationship between gas flow disturbance intensity ($\overline{u'_{gc}}/u_{gc}$), critical Karlovitz number (K_{cl}), effective Lewis number (Le_{eff}), and burnt gas Markstein number (Ma_b), helping to identify any underlying general trends or patterns.

5. Conclusions

The current research focuses on a fundamental flame-flow interaction phenomenon involving disturbances induced by flame instabilities within a premixed flame brush ahead of the flame front. It also explores the potential extension of these disturbances into the surrounding gas flow. This reassessment is grounded in experiments conducted on unstable laminar hydrogen-air outwardly propagating spherical flames within a spherical explosion vessel, carried out at both 0.1 MPa and 0.5 MPa. The Mie scattering measurement technique captures the wrinkled flame surface and resolves the local gas flow field adjacent to the flame surface front.

Flame wrinkling, stemming from intrinsic instability, plays a pivotal role in flame acceleration (self-acceleration) and gas disturbance ahead of the flame front (self-disturbance). The measurements of the self-acceleration exponent for the flame propagation speed (α) and gas flow velocity (α_g) show a close correspondence. In the case of an expanding cellularly unstable flame induced by flame instabilities, it is observed that the flow in close proximity to the flame exhibits a relatively higher RMS gas velocity. Conversely, in the distant gas field, away from the flame center, a radial mean flow predominates due to thermal dilatation, resulting in a considerably lower RMS gas velocity. The power spectral density exhibited by the gas flow preceding the flame front shows a striking resemblance to that of the own fluctuation of the flame front, suggesting that the fluctuations in gas velocity may originate from the wrinkling of the flame. Notably, the exponent demonstrated in the said power-law is roughly twice the value of the fractal dimension witnessed in the flame surface front.

Elevated pressures can result in increased gas flow disturbance intensities, particularly under lean conditions, within the region approximately 0.444 mm ahead of the flame front. Nevertheless, it is essential to recognize that within the scope of the current experiments, the

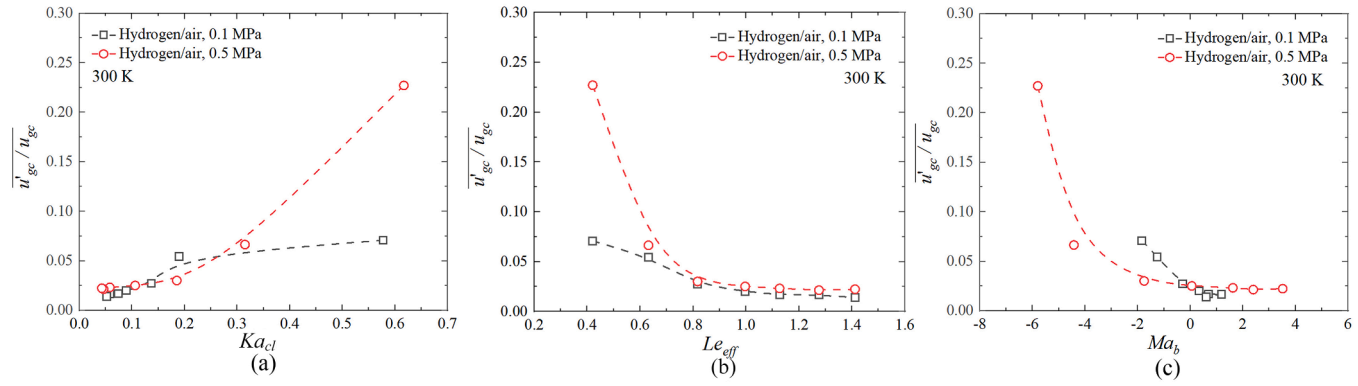

Fig. 19. Correlations of $\overline{u'_{gc}}/u_{gc}$ and K_{cl} (a), Le_{eff} (b), Ma_b (c).

disturbance intensities in the narrow zone immediately preceding the flame front remain relatively subdued when compared to scenarios characterized by genuine turbulence. Beyond the region approximately 0.444 mm from the flame front, the flow displays characteristics resembling laminar flow. In light of these observations, it can be concluded that the gas flow stemming from the wrinkled flame surface does not exhibit the typical traits of turbulent flow.

The spatial root mean square (RMS) velocity, denoted by $u_{gc}^{'}$, characterizes the disturbance intensity quantitatively around the flame surface and is observed to display oscillatory behavior around a relatively low and nearly constant value after the onset of instability. To evaluate the intrinsic disturbance intensity, $\overline{u_{gc}^{'}/u_{gc}}$ has been proposed as a normalized parameter for $u_{gc}^{'}$. Increasing $\overline{u_{gc}^{'}/u_{gc}}$ corresponds to the more wrinkled flame surface. Empirical correlations have been sought to determine $\overline{u_{gc}^{'}/u_{gc}}$ based on K_{cl}, Le_{eff} and Ma_b. Notably, there is no obvious correlation between gas flow disturbance and acceleration exponents according to this study.

CRediT authorship contribution statement

Yu Xie: Formal analysis, Investigation, Methodology, Validation, Visualization, Writing – original draft. **Junfeng Yang:** Writing – review & editing, Project administration, Funding acquisition, Supervision, Conceptualization. **Xiaojun Gu:** Writing – review & editing.

Declaration of competing interest

The authors declare that they have no known competing financial interests or personal relationships that could have appeared to influence the work reported in this paper.

Acknowledgements

Thanks are given to EPSRC (Grant No. EP/W002299/1) for financial support. Yu Xie acknowledges the China Scholarship Council and the University of Leeds for a joint PhD scholarship (CSC202008350141). Thanks are given to Dr. Mohamed E. Morsy for the valuable discussion.

Appendix A

The radial velocity of unburnt gas ahead of the flame front, u_r, is derived via a continuity equation in a 3D spherical coordinate:

$$\frac{\partial \rho}{\partial t}+\frac{1}{r^2}\frac{\partial (r^2\rho u_r)}{\partial r}=0 \tag{A.1}$$

The density of the unburnt gas away from the flame front remains nearly constant as the pressure remains unchanged, Eq. A.1 can be simplified as:

$$\frac{1}{r^2}\frac{\partial (r^2\rho u_r)}{\partial r}=0 \tag{A.2}$$

This implies $r^2\rho u_r$ is a constant. In other words:

$$r^2\rho u_r = M \tag{A.3}$$

Here M is a constant of integration, and Eq. A.3 relates r, ρ and u_r. Depending on the specific values known beforehand, this equation can determine the relationship between these variables:

$$u_r = \frac{M}{r^2\rho} \tag{A.4}$$

$$u_r(r) = \frac{X}{r^2} \tag{A.5}$$

where $X = \frac{M}{\rho}$. As a result, unburnt gas radial velocity $u_r(r)$ is a function of r.

References

[1] Y. Xie, M.E. Morsy, J. Li, J. Yang, Intrinsic cellular instabilities of hydrogen laminar outwardly propagating spherical flames, Fuel 327 (2022) 125149.
[2] Y. Xie, M.E. Morsy, J. Yang, Self-acceleration and global pulsation of unstable laminar hydrogen-air flames, Fuel 353 (2023) 129182.
[3] Z. Liu, V.R. Unni, S. Chaudhuri, R. Sui, C.K. Law, A. Saha, Self-turbulization in cellularly unstable laminar flames, J. Fluid Mech. 917 (2021).
[4] Y.A. Gostintsev, A.G. Istratov, Y.V. Shulenin, Self-similar propagation of a free turbulent flame in mixed gas mixtures, Combust. Explos. Shock Waves 24 (1988) 563–569.
[5] D. Bradley, Instabilities and flame speeds in large-scale premixed gaseous explosions, Philos. Trans. R. Soc. A 357 (1999) 3567–3581.
[6] D. Bradley, C.M. Harper, The development of instabilities in laminar explosion flames, Combust. Flame 99 (1994) 562–572.
[7] D. Bradley, C.G.W. Sheppard, R. Woolley, D.A. Greenhalgh, R.D. Lockett, The development and structure of flame instabilities and cellularity at low Markstein numbers in explosions, Combust. Flame 122 (2000) 195–209.
[8] X. Cai, J. Wang, Z. Bian, H. Zhao, H. Dai, Z. Huang, On transition to self-similar acceleration of spherically expanding flames with cellular instabilities, Combust. Flame 215 (2020) 364–375.
[9] D. Bradley, T.M. Cresswell, J.S. Puttock, Flame acceleration due to flame-induced instabilities in large-scale explosions, Combust. Flame 124 (2001) 551–559.
[10] W.K. Kim, T. Mogi, K. Kuwana, R. Dobashi, Self-similar propagation of expanding spherical flames in large scale gas explosions, Proc. Combust. Inst. 35 (2015) 2051–2058.
[11] C.R. Bauwens, J.M. Bergthorson, S.B. Dorofeev, Experimental study of spherical-flame acceleration mechanisms in large-scale propane-air flames, Proc. Combust. Inst. 35 (2015) 2059–2066.
[12] L. Filyand, G.I. Sivashinsky, M.L. Frankel, On self-acceleration of outward propagating wrinkled flames, Phys. D Nonlinear Phenom. 72 (1–2) (1994) 110–118.
[13] K. Mukaiyama, S. Shibayama, K. Kuwana, Fractal structures of hydrodynamically unstable and diffusive-thermally unstable flames, Combust. Flame 160 (11) (2013) 2471–2475.
[14] R. Yu, X.S. Bai, V. Bychkov, Fractal flame structure due to the hydrodynamic Darrieus-Landau instability, Phys. Rev. E 92 (6) (2015) 063028.
[15] F. Wu, G. Jomaas, C.K. Law, An experimental investigation on self-acceleration of cellular spherical flames, Proc. Combust. Inst. 34 (2013) 937–945.
[16] S. Yang, A. Saha, F. Wu, C.K. Law, Morphology and self-acceleration of expanding laminar flames with flame-front cellular instabilities, Combust. Flame 171 (2016) 112–118.
[17] J. Huo, A. Saha, Z. Ren, C.K. Law, Self-acceleration and global pulsation in hydrodynamically unstable expanding laminar flames, Combust. Flame 194 (2018) 419–425.
[18] S. Balusamy, A. Cessou, B. Lecordier, Direct measurement of local instantaneous laminar burning velocity by a new PIV algorithm, Exp. Fluids 50 (2011) 1109–1121.

[19] E. Varea, V. Modica, A. Vandel, B. Renou, Measurement of laminar burning velocity and Markstein length relative to fresh gases using a new postprocessing procedure: application to laminar spherical flames for methane, ethanol and isooctane-air mixtures, Combust. Flame 159 (2012) 577–590.
[20] D. Bradley, M. Lawes, M.E. Morsy, Flame speed and particle image velocimetry measurements of laminar burning velocities and Markstein numbers of some hydrocarbons, Fuel 243 (2019) 423–432.
[21] Y. Xie, J. Li, J. Yang, R. Cracknell, Laminar burning velocity blending laws using particle imaging velocimetry, Appl. Energy Combust. Sci. 13 (2023) 100114.
[22] Y. Xie, A. Lu, J. Li, J. Yang, C. Zhang, M.E. Morsy, Laminar burning characteristics of coal-based naphtha, Combust. Flame 249 (2023) 112625.
[23] X.J. Gu, D.R. Emerson, D. Bradley, Modes of reaction front propagation from hot spots, Combust. Flame 133 (2003) 63–74.
[24] G.P. Smith, D.M. Golden, M. Frenklach, N.W. Moriarty, B. Eiteneer, M. Goldenberg, C.T. Bowman, R.K. Hanson, S. Song, Jr W.C. Gardiner, V.V. Lissianski, Z. Qin, GRI 3.0 mechanism. gas research institute (1999). (http://www.me.berkeley.edu/gri_mech).
[25] D. Bradley, R.A. Hicks, M. Lawes, C.G.W. Sheppard, R. Woolley, The measurement of laminar burning velocities and Markstein numbers for iso-octane–air and iso-octane–n-heptane–air mixtures at elevated temperatures and pressures in an explosion bomb, Combust. Flame 115 (1998) 126–144.
[26] B. Karlovitz, D.W. Denniston Jr, F.E. Wells, Investigation of turbulent flames, Chem. Phys. 19 (1951) 541–547.
[27] A.C. Scurlock, J.H. Grover, Propagation of turbulent flames, Symp. (Int.) Combust. 40 (1953) 645–658.
[28] J. Chomiak, Flame-turbulence interaction, Combust. Flame 20 (1973) 143–155.
[29] J.B. Bell, N.J. Brown, M.S. Day, M. Frenklach, J.F. Grcar, S.R. Tonse, The dependence of chemistry on the inlet equivalence ratio in vortex–flame interactions, Proc. Combust. Inst. 28 (2000) 1933–1939.
[30] J.B. Bell, M.S. Day, J.F. Grcar, W.G. Bessler, C. Schultz, P. Glarborg, A.D. Jensen, Detailed modeling and laser-induced fluorescence imaging of nitric oxide in a NH3-seeded non-premixed methane/air flame, Proc. Combust. Inst. 29 (2002) 2195–2202.
[31] N. Sullivan, A. Jensen, P. Glarborg, M.S. Day, J.F. Grcar, J.B. Bell, C. Pope, R. J. Kee, Ammonia conversion and NOx formation in laminar coflowing nonpremixed methane–air flames, Combust. Flame 131 (2002) 285–298.
[32] U. Ahmed, R. Prosser, Modelling flame turbulence interaction in RANS simulation of premixed turbulent combustion, Combust. Theory Model. 20 (2016) 34–57.
[33] S. Taamallah, Y. Dagan, N. Chakroun, S.J. Shanbhogue, K. Vogiatzaki, A. F. Ghoniem, Helical vortex core dynamics and flame interaction in turbulent premixed swirl combustion: a combined experimental and large eddy simulation investigation, Phys. Fluids 31 (2019) 025108.
[34] T. Wang, X. Zhang, J. Xu, S. Zheng, X. Hou, Large-eddy simulation of flame-turbulence interaction in a spark ignition engine fueled with methane/hydrogen-carbon dioxide, Energy Convers. Manag. 104 (2015) 147–159.
[35] U. Ahmed, R. Prosser, A.J. Revell, Towards the development of an evolution equation for flame turbulence interaction in premixed turbulent combustion, Flow Turbul. Combust. 93 (2014) 637–663.
[36] A.N. Lipatnikov, V.A. Sabelnikov, S. Nishiki, T. Hasegawa, A direct numerical simulation study of the influence of flame-generated vorticity on reaction-zone-surface area in weakly turbulent premixed combustion, Phys. Fluids 31 (2019) 055101.
[37] V.A. Sabelnikov, A.N. Lipatnikov, S. Nishiki, T. Hasegawa, Application of conditioned structure functions to exploring influence of premixed combustion on two-point turbulence statistics, Proc. Combust. Inst. 37 (2019) 2433–2441.
[38] A.N. Lipatnikov, V.A. Sabelnikov, S. Nishiki, T. Hasegawa, Does flame-generated vorticity increase turbulent burning velocity? Phys. Fluids 30 (2018) 081702.
[39] A.J. Aspden, M.S. Day, J. Bell, Turbulence–flame interactions in lean premixed hydrogen: transition to the distributed burning regime, J. Fluid Mech. 680 (2011) 287–320.
[40] A.J. Aspden, M.S. Day, J.B. Bell, Turbulence-chemistry interaction in lean premixed hydrogen combustion, Proc. Combust. Inst. 35 (2) (2015) 1321–1329.
[41] A.J. Aspden, J.B. Bell, M.S. Day, F.N. Egolfopoulos, Turbulence–flame interactions in lean premixed dodecane flames, Proc. Combust. Inst. 36 (2) (2017) 2005–2016.
[42] B.D. Videto, D.A. Santavicca, Flame-turbulence interactions in a freely-propagating, premixed flame, Combust. Sci. Technol. 70 (1990) 47–73.
[43] S. Chaudhuri, A. Saha, C.K. Law, On flame–turbulence interaction in constant-pressure expanding flames, Proc. Combust. Inst. 35 (2015) 1331–1339.
[44] N. Peters, Turbulent Combustion, Cambridge University Press, 2000.
[45] D. Bradley, M. Lawes, M.E. Morsy, Combustion-induced turbulent flow fields in premixed flames, Fuel 290 (2021) 119972.
[46] Dantec, 2015. Dantec dynamic studio. https://www.dantecdynamics.com/.
[47] W. Zhang, Measurements of flow and combustion in a strongly charged spark ignition engine (Doctoral Dissertation, University of Leeds), 2018.
[48] R. Addabbo, J.K. Bechtold, M. Matalon, Wrinkling of spherically expanding flames, Proc. Combust. Inst. 29 (2002) 1527–1535.
[49] J.K. Bechtold, M. Matalon, Hydrodynamic and diffusion effects on the stability of spherically expanding flames, Combust. Flame 67 (1987) 77–90.
[50] P. Ahmed, B. Thorne, M. Lawes, S. Hochgreb, G.V. Nivarti, R.S. Cant, Three dimensional measurements of surface areas and burning velocities of turbulent spherical flames, Combust. Flame 233 (2021) 111586.